Applied Surface Science 476 (2019) 761–768

Contents lists available at ScienceDirect

Applied Surface Science

journal homepage: www.elsevier.com/locate/apsusc

Full length article

# F-doped $LiFePO_4$@N/B/F-doped carbon as high performance cathode materials for Li-ion batteries

Yanshuang Meng[a,c], Yuzhu Li[a], Jun Xia[a], Qianru Hu[a], Xinyou Ke[b], Guofeng Ren[b,*], Fuliang Zhu[a,c,**]

[a] School of Materials Science and Engineering, Lanzhou University of Technology, Lanzhou 730050, China
[b] Department of Mechanical and Aerospace Engineering, Case Western Reserve University, Cleveland, OH 44106, USA
[c] State Key Laboratory of Advanced Processing and Recycling of Non-ferrous Metals, Lanzhou 730050, China

ARTICLE INFO

*Keywords:*
F-doped $LiFePO_4$
N, B, F-doped carbon
Ionic liquids
Electrode modification
Lithium-ion batteries

ABSTRACT

$LiFePO_4$ (LFP) is widely considered as a practical cathode material for lithium ion batteries, however its applications are still plagued by the low ionic and electronic conductivities. To address this challenge, F-doped LFP coated with N, B, F ternary doped carbon layer (F-LFP@NBFC) was synthesized by hydrothermal method using ionic liquid $[BMIM]BF_4$ as the sole source for C, N, B and F. The F-LFP@NBFC exhibits superior electrochemical performance compared with the pristine LFP. F-LFP@NBFC demonstrates a discharge capacity of 162.2 mAh $g^{-1}$ at 0.1 C, which is close to its theoretical capacity, and maintains a 100% of discharge capacity after 40 cycles at 0.1 C. F-LFP@NBFC also shows an excellent rate capability and delivers a discharge capacity of 71.3 mAh $g^{-1}$ at 15 C. The excellent performance is ascribed to the surface coating of LFP and heteroatom doping into the carbon and LFP. On one hand, the N, B, F ternary doped carbon film acts as conductive network for LFP particles, improves the electronic conductivity of electrode particle and consequently enhances the $Li^+/Li^0$ reduced/oxidized kinetics. On the other hand, the crystal lattice of LFP is enlarged by the F doping, which facilitates the $Li^+$ intercalation/deintercalation. This study provides a convenient approach to prepare a high performance cathode material for lithium ion batteries.

## 1. Introduction

The energy demand in modern civilization renders the boom of energy storage technologies. New technologies, including lithium ion batteries (LIBs) [1–3], electrochemical capacitors [4–6], lithium sulfur batteries [7–10] and redox flow batteries [11,12], are emerging and rapidly developing. Due to the high energy density, portable ability and long-term cycle life [13–16], LIBs are considered as one of the most important power sources in practical applications. The commercially used cathode material, i.e. layered $LiCoO_2$, suffers from a lower safety, a more environmental toxicity and a higher capital cost than other cathode materials, such as $LiNi_xCo_yMn_zO_2$, $LiNi_xCo_yAl_zO_2$, $LiMnO_2$ and $LiFePO_4$ (LFP) [17–20]. Among these alternative cathode materials, LFP has attracted great attention because of its high safety and stability, low cost, and high theoretical capacity (170 mAh $g^{-1}$). However, the bulk LFP exhibits low specific capacity and unsatisfactory rate performance in practical use, which is attributed to its low electronic conductivity ($10^{-9}$–$10^{-10}$ S $cm^{-1}$) and sluggish transportation of $Li^+$ ions [21,22]. To improve the electrochemical properties of LFP, various methods, such as carbon coating [23,24], particle size minimization [25] and ion substitution [26,27], have been attempted to increase its electronic and ionic conductivities [28,29].

Ion substitutions in the LFP structure were reported to effectively increase the electronic conductivity and enhance the $Li^+$ kinetics of the LFP when it was used as cathode material for LIBs [30,31]. Ionic dopants in LFP lattice include cations, i.e. $Mg^{2+}$, $Cu^{2+}$, $Mn^{4+}$, $Zr^{4+}$, $Co^{2+}$, $V^{5+}$, $Zn^{2+}$, $Nb^{5+}$, $Al^{3+}$ at $Li^+$ or $Fe^{2+}$ sites [30,32–37], and anions, i.e. $F^-$, $S^{2-}$, $Cl^-$, replacing $PO_4^{3-}$ group as a whole or at $O^{2-}$ sites [38,39]. F-substitution at the oxygen site of $LiNiO_2$ was firstly reported by Kubo, in which lattice distortion could significantly increase the capacity of $LiNiO_2$ [40]. Recently, Milović et al. [39] investigated F-doped LFP by using density functional theory (DFT), and found that fluorine doping can enhance the diffusion of $Li^+$ ions and induce better conductivity properties of the doped LFP.

Carbon coating on LFP surface is another method to improve the electrochemical performance of the LFP through increasing the

* Corresponding author.
** Correspondence to: F. Zhu, School of Materials Science and Engineering, Lanzhou University of Technology, Lanzhou 730050, China.
*E-mail addresses:* gxr136@case.edu (G. Ren), chzfl@126.com (F. Zhu).

https://doi.org/10.1016/j.apsusc.2019.01.139
Received 26 October 2018; Received in revised form 8 January 2019; Accepted 18 January 2019
Available online 20 January 2019
0169-4332/ 

electronic conductivity, providing mechanical protection to LFP particles and preventing LFP particles from agglomeration during the charge/discharge process [41]. Introduction of heteroatoms, i.e. N, S, B, P, F, etc., into the carbon film can further improve the electrochemical performance of the composites because heteroatoms can not only act as electron donors to provide charge carriers [42], but also induce a high amount of defects and therefore facilitate the $Li^+$ transport in the carbon film [43]. Binary or ternary heteroatom doping in carbon displayed a synergetic effect in enhancing electrochemical properties of carbon materials. For examples, N, B, F ternary doped carbon fibers exhibited higher kinetic activity and stability compared with the single N-doped carbon fibers used in Zinc-Air batteries [44]. LFP coated with N, B, F ternary doped carbon layer exhibited improved electrochemical performance than that of the single N- or B-doped materials [45]. However, how to prepare ternary heteroatom doped carbon film on the surface of the electrode material remains a great challenge.

Ionic liquids (ILs) are widely used as carbon sources to form heteroatom doped carbon layer on LFP due to that ILs can penetrate into porous crystals, and subsequently form a thin and uniform film on the surface of LFP particles [46,47]. Furthermore, heteroatoms, i.e. N, S, B, P, F, etc., originally from ILs remain in the pyrolyzed carbon and enable the formation of the heteroatom doped carbon films on the surface of LFP particles [48]. In our previous work [49], the IL 1-butyl-3-methylimidazolium dicyanamide was used as both carbon and heteroatom source to prepare N-doped carbon film on the surface of LFP. A high discharge capacity of 160.6 mAh $g^{-1}$ after 50 cycles at 0.1 C and a discharge capacity of 143.6 mAh $g^{-1}$ at 1 C were achieved.

In this work, we present a convenient approach to prepare F-doped LFP coated with N, B, F ternary doped carbon film (F-LFP@NBFC). Ionic liquid 1-butyl-3-methylimidazolium tetrafluoroborate ([BMIM]$BF_4$) was employed as the sole source for carbon and heteroatom (N, B and F) dopants in both NBFC and F-LFP simultaneously. F-LFP@NBFC was synthesized by a one-step hydrothermal reaction using the ionic liquid [BMIM]$BF_4$. [BMIM]$BF_4$ was pyrolyzed during the heat treatment process, which formed N, B, F ternary doped carbon film on the surface of LFP particles. F element from [BMIM]$BF_4$ simultaneously doped into the lattice of the LFP. The characterization results showed that F doping led to an expansion of lattice parameters *b* and *c* of the LFP, which enhanced the $Li^+$ intercalation/de-intercalation kinetics. The N, B, F ternary doped carbon film on the surface of LFP particles increased the conductivity of LFP and $Li^+$ transport. As a result, the F-LFP@NBFC exhibited excellent electrochemical performance in LIBs.

## 2. Experimental approaches

### 2.1. Synthesis of F-LFP@NBFC

An illustration of synthesizing the F-LFP@NBFC is shown in Fig. 1. LFP was synthesized by the hydrothermal method reported in literature [49]. In a typical synthesis process, the stoichiometric amounts of $LiOH{\cdot}H_2O$ (98%), $H_3PO_4$ (85%), and $FeSO_4{\cdot}7H_2O$ (99%) (molar ratio is 3:1:1) were dissolved in distilled water. The solution was stirred for 0.5 h. The solution was then transferred into a 200 mL Teflon-lined stainless steel autoclave and maintained at a temperature of 180 °C for 10 h. After cooling down to the room temperature, the obtained gray dark slurry was centrifugally washed three times by the deionized water/absolute alcohol, and eventually dried at 110 °C for 12 h. The dark gray slurry became the dark gray powder, which was further treated in the argon at 700 °C for 10 h to synthesize the pristine LFP. To synthesize F-LFP@NBFC, the IL [BMIM]$BF_4$ (30 wt%) was dropped into the LFP and stirred for 30 min and a new slurry was obtained. This slurry was dried and calcined in the argon at 700 °C for 10 h. After cooling down to the room temperature, the F-LFP@NBFC sample was eventually obtained.

### 2.2. Structure and morphology characterizations

XRD characterization for the LFP and F-LFP@NBFC was performed using a Rigaku D/max-2500 with the Cu Kα radiation (λ = 0.15406 nm) in the 2θ range from 10° to 80° at room temperature. Raman spectra were obtained from a LabRAM HR UV/vis/NIR (Horiba Jobin Yvon) with a He-Ne laser (excitation line 532 nm). JEOL-7500F scanning electron microscopy (SEM) and JEOL-JEM-2010F transmission electron microscopy (TEM) were employed to characterize the morphologies and microstructures of the materials. Energy dispersive spectroscopy (EDS) on the SEM was used to probe the chemical contents of the materials. The X-ray photoelectron spectroscopy (XPS) analysis was performed on a PHI-5702 multifunctional photoelectron spectrometer with an analyzer pass energy of 29.4 eV.

### 2.3. Electrochemical characterization

Coin type half-cells were assembled for the electrochemical tests. The working electrodes were prepared by using LFP (or F-LFP@NBFC) as the active material, polyvinylidene fluoride (PVDF) as the binder and Super-P as the conductive agent with a weight ratio of 8:1:1. Three of them were well mixed in an appropriate amount of *N*-methyl-2-pyrrolidone by stirring to obtain a uniform slurry which was then coated onto a piece of aluminum foil. The coated aluminum foil was dried in the vacuum at 110 °C for 10 h. The mass loading for the electrodes is about 1.0 mg $cm^{-2}$. Half-cells were assembled inside a glove box using 1 M $LiPF_6$ in a solvent mixture of EC:DEC (1:1, vol%) as the electrolyte. The cycling and rate capability tests were conducted by a Land CT2001A battery tester. The half-cells were charged and discharged with desired constant currents in a voltage window of 2.5 to 4.2 V. Cyclic voltammetry (CV) was performed with a Chi660E electrochemical workstation

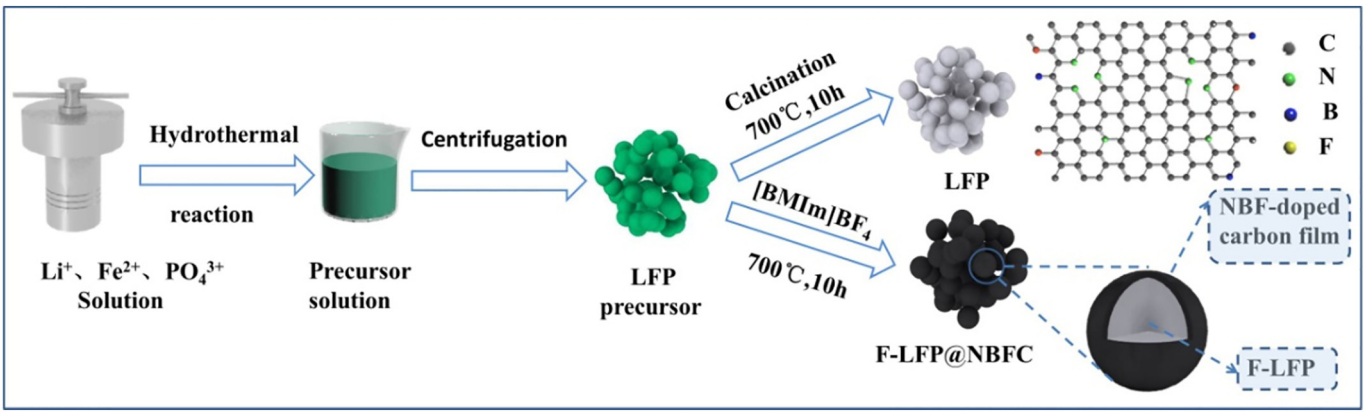


**Fig. 1.** An illustration of synthesizing F-LFP@NBFC.

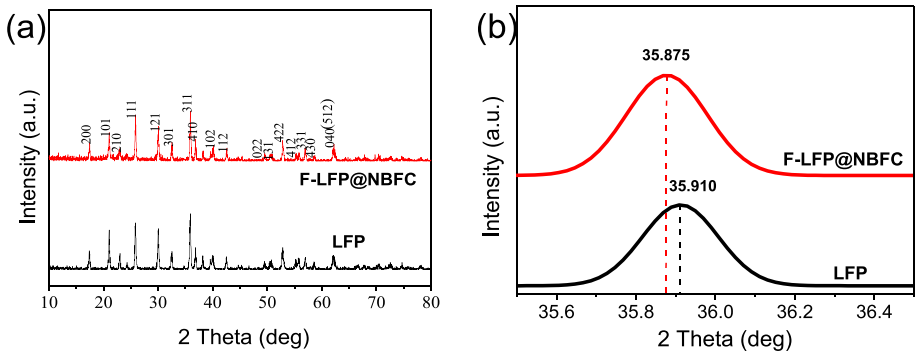


**Fig. 2.** XRD patterns of the LFP and the F-LFP@NBFC.

at scan rates between 0.1 mV $s^{-1}$ and 5 mV $s^{-1}$. Electrochemical impedance spectroscopy (EIS) was measured by a Chi660E electrochemical workstation in the frequency ranging from 0.01 Hz to 100 kHz with a sinusoidal amplitude of 5 mV at the open circuit voltage with 0 V voltage bias.

## 3. Results and discussion

### 3.1. Analysis of structure and morphology

XRD patterns of the LFP and F-LFP@NBFC samples are shown in Fig. 2. The characteristic peaks from both LFP and F-LFP@NBFC can be indexed to the crystal of LFP (JCPDS 40-1499), which has an orthorhombic structure and belongs to the *Pnma* space group. There are no characteristic peaks from carbon, indicating that the content of the carbon in the F-LFP@NBFC is extremely low. Fig. 2(b) shows the magnification peak for the 2θ range of 35.5–36.5°. It can be seen that the peak from the F-LFP@NBFC has a slight shift to a lower angle compared with that from the LFP, which indicates that F-LFP@NBFC has a larger unit cell volume than LFP [50]. The calculated crystal lattice parameters of the LFP and the F-LFP@NBFC are summarized in Table 1. A slight expansion of the unit cell volume reveals that the insertion of F element can cause a distortion of the LFP, which improves the rate performance and cycle ability of LFP [31,51].

The morphology and particle size of the LFP and F-LFP@NBFC were examined by SEM. Fig. 3(a) shows that the LFP particles have a diameter ranging from 1 μm to 5 μm. The SEM image of the F-LFP@NBFC, as shown in Fig. 3(b), reveals that the particles of the F-LFP@NBFC have a diameter ranging from 1 μm to 5 μm, indicating that the carbon coating process does not alter the particle size distribution of the F-LFP@NBFC. EDS mapping images as shown in Fig. 3(c), suggest that Fe, P and O distribute uniformly in the F-LFP@NBFC particles. The F element also distributes on the surface of the F-LFP@NBFC particles and it confirms that F was doped into the carbon and/or the crystal of LFP. The C distribution reveals that a uniform carbon film was formed on the surface of LFP particles. In addition, N and B distributions vary with the morphology of the carbon film, which indicates that N and B may coexist in the carbon layer. TEM and HRTEM were used to further investigate the microstructures of the LFP, the F-LFP@NBFC and the superficial carbon film and the obtained images are shown in Fig. 4. It can be seen that a uniform carbon film is formed on the surface of the LFP with a thickness of 5–6 nm (Fig. 4(d)).

Raman spectrum was used to analyze the microstructures of the carbon film on the surface of the F-LFP@NBFC as shown in Fig. 5(a). The band located at 953 $cm^{-1}$ is assigned to the symmetric stretch of P—O [52]. The bands below 400 $cm^{-1}$ are assigned to the translation of Fe and $PO_4^{3-}$ and vibration of Fe—O [53]. Four bands at the 1210 $cm^{-1}$, 1360 $cm^{-1}$, 1510 $cm^{-1}$ and 1590 $cm^{-1}$ are obtained after Gauss fitting of the Raman spectrum as shown in Fig. 5(a). The bands located at the 1210 $cm^{-1}$ and 1510 $cm^{-1}$ are generally assigned to $sp^3$-coordinated carbonaceous materials, and the bands at the 1360 $cm^{-1}$ and 1590 $cm^{-1}$ are attributed to the $sp^2$-coordinated graphite structured carbon [54,55]. The corresponding ratio of $I_{1360}/I_{1210}$ and $I_{1590}/I_{1510}$ are 2.86 and 2.29, which indicate that F-LFP@NBFC has a higher amount of $sp^2$-coordinated carbon than the $sp^3$-coordinated carbon. This suggests a high conductivity of carbon film on the surface of the F-LFP@NBFC and consequently improved electrochemical performance of the F-LFP@NBFC.

Fig. 5(b) shows the XPS spectrum of the F-LFP@NBFC, the peaks at binding energy of 58.3 eV, 135.8 eV, 192.9 eV, 287.9 eV, 400.1 eV, 688.8 eV and 715.5 eV correspond to Li1s, P2p, B1s, C1s, N1s, F1s and Fe2p, respectively. Fig. 5(c) is the high-resolution XPS spectra of C1s for the F-LFP@NBFC. The fitting peaks at 284.6 eV, 285.1 eV and 287.3 eV are attributed to the $sp^2$-coordinated carbon, the $sp^3$-coordinated carbon and C=O coordinated carbon, respectively [56,57]. The N1s spectrum as shown in Fig. 5(d), is de-convoluted into three peaks at 399.2 eV, 400.5 eV and 401.3 eV, which are relevant to the configuration of pyridinic N, pyrrolic N and graphitic N, respectively [58]. Two peaks at 685.9 eV and 688.1 eV are introduced in the fitting of the F1s spectra as shown in Fig. 5(e), and correspond to the F—Li and F—C, respectively [59]. The presence of the F—Li bond confirms that F-element was incorporated into the LFP lattice. In the high-resolution XPS spectrum of B1s as shown in Fig. 5(f), the peak at 189.1 eV corresponds to $BC_3$ and the peak at 191.4 eV corresponds to $BC_2O$ [60,61], indicating that the B atom bound is not only with C but also with O [62]. Boron atoms tend to break carbon atoms to form dangling bonds at the edge of carbon film, and finally lead to defects [63]. Table 2 lists the distributions of the bond types for the F-LFP@NBFC. The appearance of C—N, B—C and C—F bonds confirms that the carbon film was ternary-doped with N, B and F. There is no N—B signal in the N1s spectrum (397.9 eV) neither in the B1s spectrum (190.1 eV), indicating that the nonconductive B—N pairs were not formed in the carbon film. The F doping in the LFP lattice and the ternary doping in the carbon film synergistically facilitate the electron conduction and $Li^+$ transport in the F-LFP@NBFC. Therefore, the F-LFP@NBFC is expected to exhibit high electrochemical performance.

**Table 1**
Lattice parameters of the LFP and the F-LFP@NBFC.

| Sample | a/Å | b/Å | c/Å | V/Å$^3$ |
|---|---|---|---|---|
| LFP | 10.30425 | 5.93397 | 4.68391 | 286.40 |
| F-LFP@NBFC | 10.25402 | 5.95417 | 4.69365 | 286.57 |

### 3.2. Electrochemical properties

The initial CVs of the LFP and the F-LFP@NBFC at a scan rate of 0.1 mV $s^{-1}$ are shown in Fig. 6(a). The redox peak at 3.29/3.58 V is observed for the LFP and the peak at 3.24/3.62 V is observed for the F-LFP@NBFC. CV curves from the half-cell based on the F-LFP@NBFC

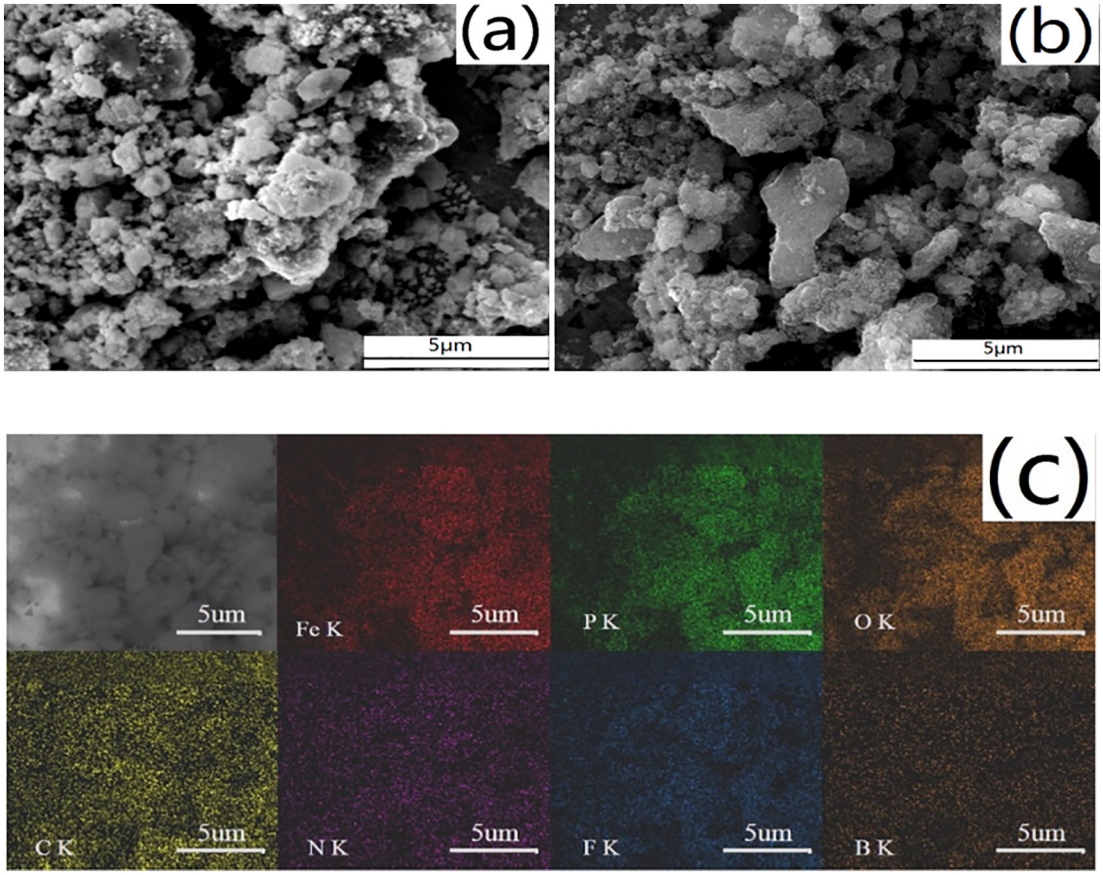


**Fig. 3.** (a) SEM image of LFP; (b) SEM image of F-LFP@NBFC; (c) EDS mappings of F-LFP@NBFC.

exhibit sharper peaks, higher peak intensity and larger enclosed area than that from the half-cell based on the LFP, suggesting enhanced electrochemical kinetics of intercalation/de-intercalation of $Li^+$ into/from the F-LFP@NBFC. Fig. 6(b) shows the first ten CV curves at a scan rate of 0.1 mV $s^{-1}$ for the F-LFP@NBFC. The CV curves are roughly overlapped with each other, demonstrating that the F-LFP@NBFC has improved cycling stability and reversibility, which are attributed to the synergistic effect of the ternary doping in the carbon film and the F doping in the LFP lattice. On one hand, the N, B and F dopants in the carbon film not only improve the electronic conductivity of the carbon

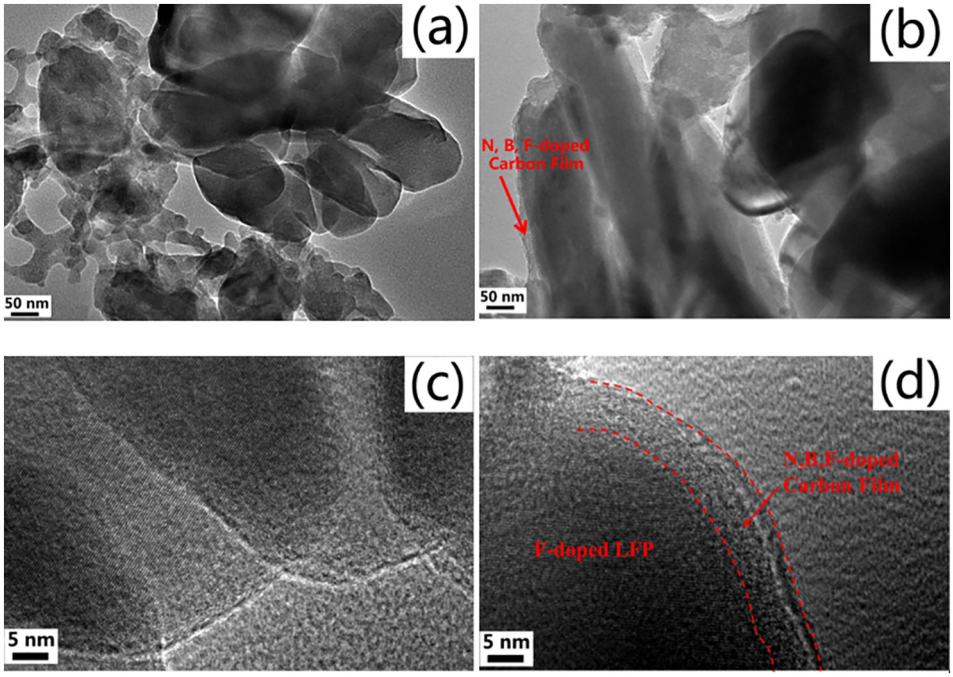


**Fig. 4.** TEM images of LFP (a) and F-LFP@NBFC (b); HRTEM images of LFP (c) and F-LFP@NBFC (d).

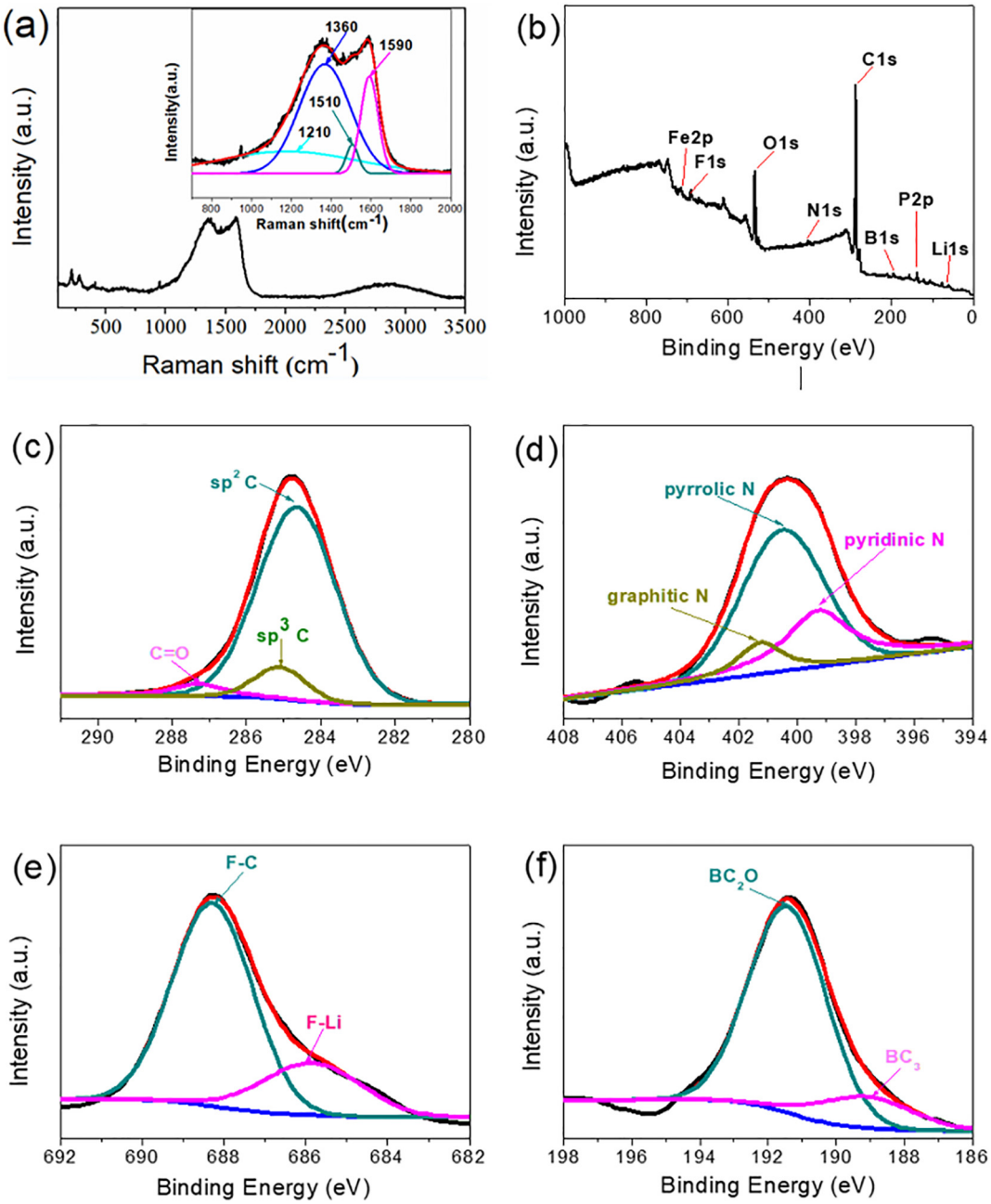


**Fig. 5.** Raman spectra (a), XPS spectrum (b), and high-resolution spectra of C1s, N1s, F1s and B1s (c–f) for the F-LFP@NBFC.

**Table 2**
Distribution of bond types of F-LFP@NBFC.

| Atom | Emission peak | Binding energy/eV |
|---|---|---|
| C | $sp^2$ C | 284.6 |
| | $sp^3$ C | 285.1 |
| | C=O | 287.3 |
| N | Pyridinic N | 399.2 |
| | Pyrrolic N | 400.5 |
| | Graphitic N | 401.3 |
| F | F–Li | 685.9 |
| | F–C | 688.1 |
| B | B–C | 189.1 |
| | B–C–O | 191.4 |

film through changing the electronic structure of the carbon [64,65], but also boost $Li^+$ intercalation/de-intercalation kinetics in the carbon film by providing deficiencies and vacancies, which facilitate $Li^+$ penetration [59,66]. On the other hand, F dopant modifies the microstructures of the LFP by weakening the Li–O bonds and therefore improves the $Li^+$ diffusion in the LFP, which enables F-doped LFP to exhibit a stable cycle ability and a high rate performance [51]. CV curves of the F-LFP@NBFC as shown in Fig. 6(c) demonstrate that redox potentials are 0.26 V, 0.32 V, 0.36 V, 0.4 V, 0.51 V and 0.71 V with respect to scan rates of 0.1 mV $s^{-1}$, 0.2 mV $s^{-1}$, 0.5 mV $s^{-1}$, 1 mV $s^{-1}$, 2 mV $s^{-1}$ and 5 mV $s^{-1}$, respectively.

To further analyze the characteristics of the LFP and the F-LFP@NBFC, the EIS was conducted in a frequency range of 0.01 Hz–100 kHz with an amplitude of 5 mV, as shown in Fig. 6(d). The semicircle at high-frequency region corresponds to the charge-transfer resistance, and the straight line at lower frequency represents the $Li^+$ diffusion

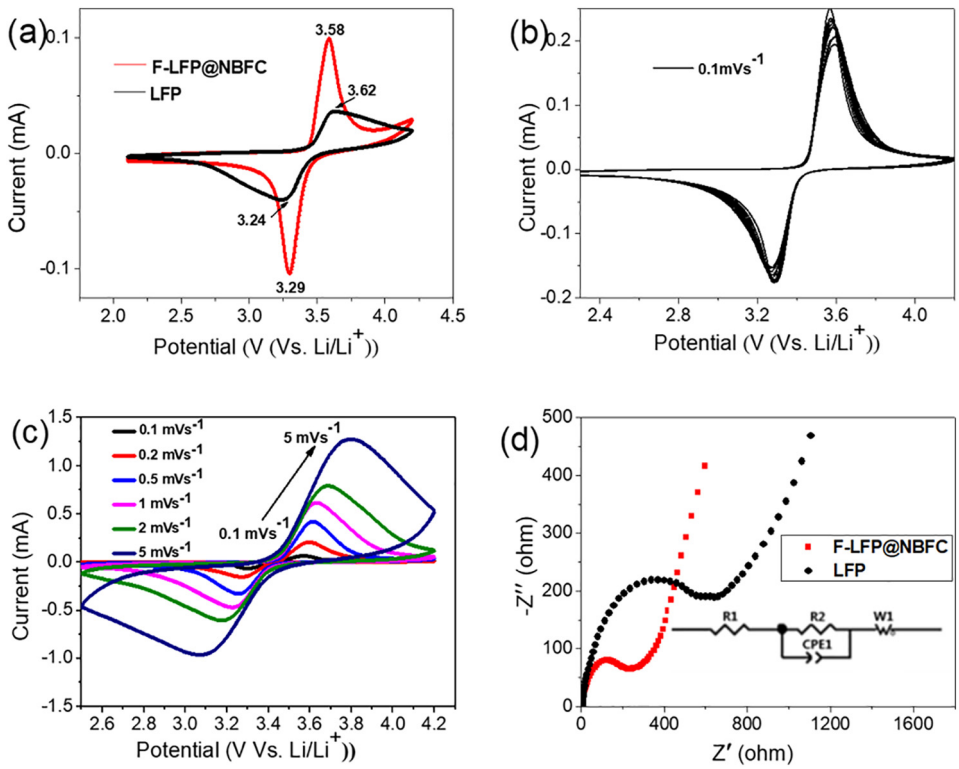


**Fig. 6.** (a) CV curves of the LFP and F-LFP@NBFC at a scan rate of 0.1 mV $s^{-1}$; (b) first ten CV curves of the F-LFP@NBFC at a scan rate of 0.1 mV $s^{-1}$; (c) CV curves of the F-LFP@NBFC at different scan rates; (d) Nyquist plots of the LFP and F-LFP@NBFC with a frequency range of 0.01 Hz–100 kHz.

from the surface into the interior of the crystalline LFP or F-LFP@NBFC (Warburg impedance) [45,67]. A smaller radius for the F-LFP@NBFC reveals a smaller charge-transfer resistance [66]. The EIS data is fitted through the equivalent circuit and as shown in Fig. 6(d). R1 refers to the uncompensated resistance, including particle-particle contact resistance, electrolyte resistance, and the resistance between the electrode and the current collector [67]. R2 represents the charge-transfer resistance, and W1 refers to the Warburg impedance. Based on the equivalent circuit, the charge-transfer resistance of the F-LFP@NBFC is fitted to be 240 Ω, which is much lower than that of LFP (655 Ω). The smaller charge-transfer resistance of the F-LFP@NBFC is attributed not only to the improved electrical conductivity of the N, B, F ternary doped carbon film which acts as conductive network [68,69], but also to the enhanced conductivity of the F-LFP@NBFC caused by the F doping in LFP lattice [70].

Charge/discharge curves of the LFP and F-LFP@NBFC are shown in Fig. 7. The initial voltage profile at a charge/discharge rate of 0.1 C shown in Fig. 7(a) displays that the F-LFP@NBFC delivers a discharge capacity of 161.9 mAh $g^{-1}$ with a coulombic efficiency of 96.5%, which is significantly higher than those of the pristine LFP with a discharge capacity of 50.7 mAh $g^{-1}$ and a coulombic efficiency of 63.6%. Also, the F-LFP@NBFC shows a lower charge voltage plateau and a higher discharge voltage plateau compared with the LFP. In other words, the F-LFP@NBFC has a lower polarization potential of 30 mV than that of LFP (200 mV). It might be attributed to the enhanced conductivity of the F-LFP@NBFC resulted from the uniformly bonded carbon film on its surface [71]. A higher discharge voltage plateau means the F-LFP@NBFC can deliver more energy, which consequently improves the energy density of the batteries [72,73].

Fig. 7(b) shows that the initial charge/discharge capacities of the F-LFP@NBFC at different rates are 167.8/161.9 mAh $g^{-1}$ (0.1 C), 156.1/154.1 mAh $g^{-1}$ (0.3 C), 147.4/143.6 mAh $g^{-1}$ (1 C), 140.3/134.2 mAh $g^{-1}$ (3 C) and 123.8/116.4 mAh $g^{-1}$ (5 C), respectively. The rate performance of the F-LFP@NBFC is shown in Fig. 7(c), the average discharge capacities are 161.5 mAh $g^{-1}$, 156.6 mAh $g^{-1}$, 147.9 mAh $g^{-1}$, 141.7 mAh $g^{-1}$, 123.9 mAh $g^{-1}$ and 71.3 mAh $g^{-1}$ at 0.1 C, 0.3 C, 1 C, 3 C, 5 C and 15 C, respectively. The discharge capacity goes back to 164 mAh $g^{-1}$ when the charge/discharge rate returns to 0.1 C. It confirms that the F-LFP@NBFC has good rate capability and stability. However, the average discharge capacities of the pristine LFP are 47.1 mAh $g^{-1}$, 41.6 mAh $g^{-1}$, 31.5 mAh $g^{-1}$, 24.7 mAh $g^{-1}$ and 10.6 mAh $g^{-1}$ at 0.1 C, 0.2 C, 0.5 C, 1 C and 5 C, respectively. Clearly, the F-LFP@NBFC exhibits a superior electrochemical performance compared with the pristine LFP. The long-term cycling performance of the LFP and F-LFP@NBFC are showed in the Fig. 7(d). It can be seen that the F-LFP@NBFC has a specific capacity of 162.2 mAh $g^{-1}$ after 40 cycles, and a 100% of the discharge capacity is maintained. While the pristine LFP demonstrates a capacity of 44.3 mAh $g^{-1}$ after 40 cycles, and only 87% of the discharge capacity is maintained. The Coulombic efficiency of F-LFP@NBFC was also improved. The enhanced cycling performance may be originated from F doping and carbon coating. F doping enlarges the unit cell volume of the LFP and improves the accessibility of the $Li^+$, which could sustain the stability of the crystal structure of LFP during cycling. In addition, carbon layer on the surface of LFP particles provides a mechanical protection.

## 4. Conclusion

F-doped LFP coated with N, B and F ternary doped carbon film (F-LFP@NBFC) was synthesized using ionic liquid $[BMIM]BF_4$ as the sole source of C, N, B and F. It was demonstrated that the F-LFP@NBFC has an improved electrochemical performance compared with pristine LFP. F-LFP@NBFC can deliver a discharge capacity of 162.2 mAh $g^{-1}$ and 71.3 mAh $g^{-1}$ at 0.1 C and 15 C, respectively. It also can maintain a 100% of discharge capacity after 40 cycles at a discharge rate of 0.1 C. The improved performance is attributed to the increased conductivity and mechanical protection by the carbon coating and a more accessibility of $Li^+$ by the enlarged crystal lattice of the LFP.

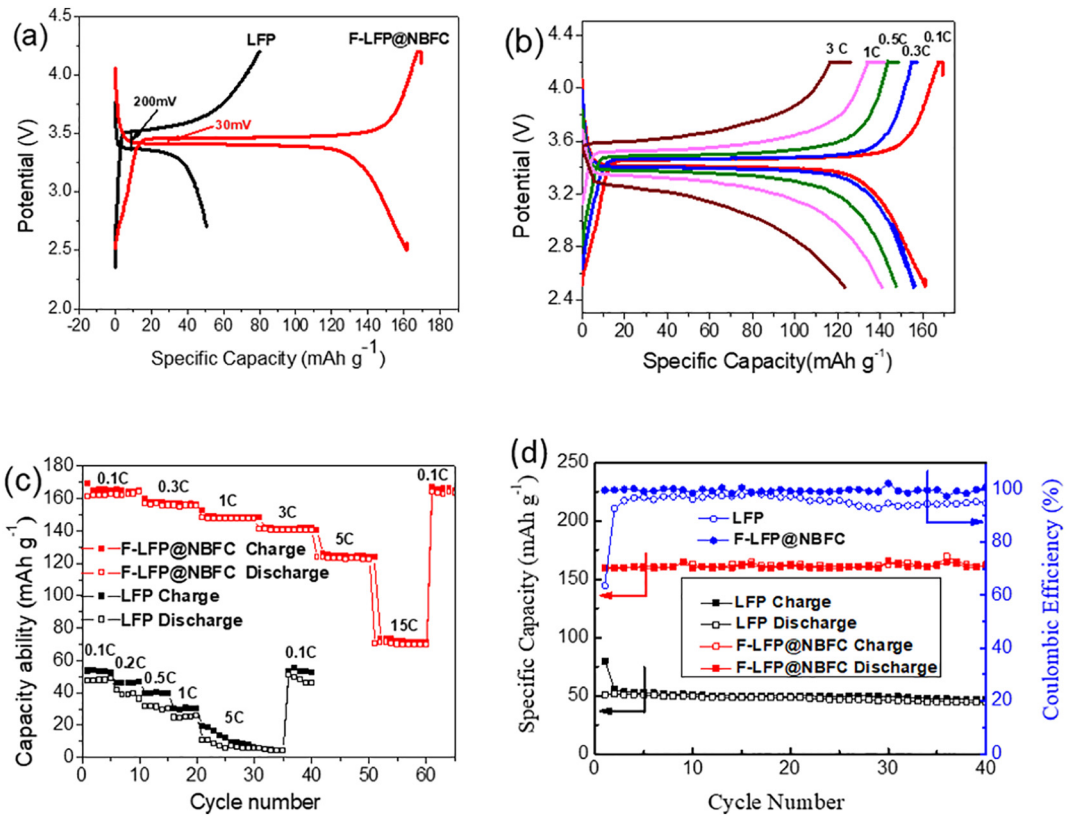


**Fig. 7.** (a) The initial voltage profiles of the LFP and F-LFP@NBFC at a charge/discharge rate of 0.1 C; (b) the charge/discharge curves at various rates for the F-LFP@NBFC; (c) rate capability of the LFP and F-LFP@NBFC; (d) cycling performance of the LFP and F-LFP@NBFC at a charge/discharge rate of 0.1 C.

## Acknowledgements

The authors thank the National Natural Science Foundation of China (NFSC) (grant No. 51364024, 51404124) and the Foundation for Innovation Groups of Basic Research in Gansu Province (No. 1606RJIA322) for financial support.

## Declarations of interest

None.

## References

[1] L. Croguennec, M.R. Palacin, Recent achievements on inorganic electrode materials for lithium-ion batteries, J. Am. Chem. Soc. 137 (9) (2015) 3140–3156.
[2] V. Etacheri, R. Marom, R. Elazari, G. Salitra, D. Aurbach, Challenges in the development of advanced Li-ion batteries: a review, Energy Environ. Sci. 4 (9) (2011) 3243–3262.
[3] N. Nitta, F. Wu, J.T. Lee, G. Yushin, Li-ion battery materials: present and future, Mater. Today 18 (5) (2015) 252–264.
[4] G. Ren, X. Pan, S. Bayne, Z. Fan, Kilohertz ultrafast electrochemical supercapacitors based on perpendicularly-oriented graphene grown inside of nickel foam, Carbon 71 (2014) 94–101.
[5] X. Pan, G. Ren, M.N.F. Hoque, S. Bayne, K. Zhu, Z. Fan, Fast supercapacitors based on graphene-bridged V2O3/VOx core–shell nanostructure electrodes with a power density of 1 MW kg−1, Adv. Mater. Interfaces 1 (9) (2014) 1400398.
[6] Y. Wang, Y. Song, Y. Xia, Electrochemical capacitors: mechanism, materials, systems, characterization and applications, Chem. Soc. Rev. 45 (21) (2016) 5925–5950.
[7] Q. Pang, X. Liang, C.Y. Kwok, L.F. Nazar, Advances in lithium–sulfur batteries based on multifunctional cathodes and electrolytes, Nat. Energy 1 (9) (2016) 16132.
[8] S. Li, T. Mou, G. Ren, J. Warzywoda, Z. Wei, B. Wang, et al., Gel based sulfur cathodes with a high sulfur content and large mass loading for high-performance lithium–sulfur batteries, J. Mater. Chem. A 5 (4) (2017) 1650–1657.
[9] S. Li, T. Mou, G. Ren, J. Warzywoda, B. Wang, Z. Fan, Confining sulfur species in cathodes of lithium–sulfur batteries: insight into nonpolar and polar matrix surfaces, ACS Energy Lett. 1 (2) (2016) 481–489.
[10] A. Manthiram, Y. Fu, S.-H. Chung, C. Zu, Y.-S. Su, Rechargeable lithium–sulfur batteries, Chem. Rev. 114 (23) (2014) 11751–11787.
[11] X. Ke, J.M. Prahl, J.I.D. Alexander, J.S. Wainright, T.A. Zawodzinski, R.F. Savinell, Rechargeable redox flow batteries: flow fields, stacks and design considerations, Chem. Soc. Rev. 47 (2018) 8721–8743.
[12] X. Ke, J.I.D. Alexander, J.M. Prahl, R.F. Savinell, Flow distribution and maximum current density studies in redox flow batteries with a single passage of the serpentine flow channel, J. Power Sources 270 (2014) 646–657.
[13] M. Li, J. Lu, Z. Chen, K. Amine, 30 years of Lithium-ion Batteries, Adv. Mater. (2018) e1800561.
[14] Q. Wang, J. Kang, Z. Tan, M. Luo, An online method to simultaneously identify the parameters and estimate states for lithium ion batteries, Electrochim. Acta 289 (2018) 376–388.
[15] G. Ren, M.N.F. Hoque, X. Pan, J. Warzywoda, Z. Fan, Vertically aligned VO2 (B) nanobelt forest and its three-dimensional structure on oriented graphene for energy storage, J. Mater. Chem. A 3 (20) (2015) 10787–10794.
[16] G. Ren, M.N.F. Hoque, J. Liu, J. Warzywoda, Z. Fan, Perpendicular edge oriented graphene foam supporting orthogonal TiO2 (B) nanosheets as freestanding electrode for lithium ion battery, Nano Energy 21 (2016) 162–171.
[17] Y. Yu, J. Wang, P. Zhang, J. Zhao, A detailed thermal study of usual $LiNi_{0.5}Co_{0.2}Mn_{0.3}O_2$, $LiMn_2O_4$ and $LiFePO_4$ cathode materials for lithium ion batteries, J. Energy Storage 12 (2017) 37–44.
[18] Y. Cho, M.H. Lee, H. Kim, K. Ku, G. Yoon, S.-K. Jung, et al., Activating layered $LiNi_{0.5}Co_{0.2}Mn_{0.3}O_2$ as a host for Mg intercalation in rechargeable Mg batteries, Mater. Res. Bull. 96 (2017) 524–532.
[19] D.-C. Li, H. Noguchi, M. Yoshio, Electrochemical characteristics of $LiNi_{0.5-x}Mn_{0.5-x}Co_{2x}O_2$ ($0 < x \leq 0.1$) prepared by spray dry method, Electrochim. Acta 50 (2–3) (2004) 427–430.
[20] J. Liu, Z. Sun, J. Xie, H. Chen, N. Wu, B. Wu, Synthesis and electrochemical properties of $LiNi_{0.5-x}Cu_xMn_{1.5-y}Al_yO_4$ (x = 0, 0.05, y = 0, 0.05) as 5 V spinel materials, J. Power Sources 240 (2013) 95–100.
[21] L.-X. Yuan, Z.-H. Wang, W.-X. Zhang, X.-L. Hu, J.-T. Chen, Y.-H. Huang, et al., Development and challenges of $LiFePO_4$ cathode material for lithium-ion batteries, Energy Environ. Sci. 4 (2) (2011) 269–284.
[22] J. Wang, Y. Niu, Y. Fu, Y. Yang, M. Hojamberdiev, Urea and ethylene glycol-assisted solvothermal synthesis of spheroidal $LiFePO_4$/C nanoparticles as a cathode material for lithium-ion batteries, ChemistrySelect 3 (19) (2018) 5471–5479.
[23] Y.G. Huang, F.H. Zheng, X.H. Zhang, Q.Y. Li, H.Q. Wang, Effect of carbon coating on cycle performance of LiFePO4/C composite cathodes using Tween80 as carbon source, Electrochim. Acta 130 (4) (2014) 740–747.
[24] Q.B. Liu, S.J. Liao, H.Y. Song, Z.X. Liang, High-performance LiFePO4/C materials: effect of carbon source on microstructure and performance, J. Power Sources 211 (211) (2012) 52–58.
[25] ZhanXu Yang, QingDong Qiao, XiaoXue Kang, et al., Facile synthesis of nanostructured LiFePO4/C cathode material for lithium-ion batteries, Sci. Bull. 57 (32)

(2012) 4160–4163.
[26] Z. Huang, Y. Xu, C. Zhao, Y. Xu, Q. Jiang, Effects of carbon coating and metal ions doping on low temperature electrochemical properties of LiFePO 4 cathode material, Electrochim. Acta 83 (12) (2012) 341–347.
[27] D. Wang, H. Li, S. Shi, X. Huang, L. Chen, Improving the rate performance of LiFePO4 by Fe-site doping, Electrochim. Acta 50 (14) (2005) 2955–2958.
[28] H.C. Shin, W.I. Cho, H. Jang, Electrochemical properties of the carbon-coated $LiFePO_4$ as a cathode material for lithium-ion secondary batteries, J. Power Sources 159 (2) (2006) 1383–1388.
[29] Y. Gao, K. Chen, H. Chen, X. Hu, Z. Deng, Z. Wei, Surfactant assisted solvothermal synthesis of $LiFePO_4$ nanorods for lithium-ion batteries, J. Energy Chem. 26 (3) (2017) 564–568.
[30] L. Gao, Z. Xu, S. Zhang, J. Xu, K. Tang, Enhanced electrochemical properties of $LiFePO_4$ cathode materials by Co and Zr multi-doping, Solid State Ionics 305 (2017) 52–56.
[31] T.-t. Zhan, C. Li, Y.-x. Jin, S.-h. Xiao, Enhanced electrochemical performances of $LiFePO_4$/C via V and F Co-doping for lithium-ion batteries, Chin. J. Chem. Phys. 29 (3) (2016) 303–307.
[32] R. Gupta, S. Saha, M. Tomar, V.K. Sachdev, V. Gupta, Effect of manganese doping on conduction in olivine $LiFePO_4$, J. Mater. Sci. Mater. Electron. 28 (7) (2017) 5192–5199.
[33] S.Y. Chung, Y.M. Chiang, Microscale measurements of the electrical conductivity of doped LiFePO4, Electrochem. Solid-State Lett. 6 (12) (2003) A278–A281.
[34] X. Hui, Z. Zhou, Physical and electrochemical properties of mix-doped lithium iron phosphate as cathode material for lithium ion battery, Electrochim. Acta 51 (10) (2006) 2063–2067.
[35] C.Y. Chiang, H.C. Su, P.J. Wu, H.J. Liu, C.W. Hu, N. Sharma, et al., Vanadium substitution of LiFePO4 cathode materials to enhance the capacity of LiFePO4-based lithium-ion batteries, J. Phys. Chem. C 116 (46) (2012) 24424–24429.
[36] H. Liu, Q. Cao, L.J. Fu, C. Li, Y.P. Wu, H.Q. Wu, Doping effects of zinc on LiFePO cathode material for lithium ion batteries, Electrochem. Commun. 8 (10) (2006) 1553–1557.
[37] J.F. Ni, H.H. Zhou, J.T. Chen, X.X. Zhang, LiFePO4 doped with ions prepared by co-precipitation method, Mater. Lett. 59 (18) (2005) 2361–2365.
[38] C.S. Sun, Y. Zhang, X.J. Zhang, Z. Zhou, Structural and electrochemical properties of Cl-doped LiFePO4/C, J. Power Sources 195 (11) (2010) 3680–3683.
[39] M. Milović, D. Jugović, N. Cvjetićanin, D. Uskoković, A.S. Milošević, Z.S. Popović, et al., Crystal structure analysis and first principle investigation of F doping in $LiFePO_4$, J. Power Sources 241 (2013) 70–79.
[40] K. Kubo, M. Fujiwara, S. Yamada, S. Arai, M. Kanda, Synthesis and electrochemical properties for LiNiO2 substituted by other elements, J. Power Sources 68 (2) (1997) 553–557.
[41] Q. Xiong, C. Zheng, H. Chi, J. Zhang, Z. Ji, Reconstruction of $TiO_2$/$MnO_2$-C nanotube/nanoflake core/shell arrays as high-performance supercapacitor electrodes, Nanotechnology 28 (5) (2016) 055405.
[42] C. Wang, Z. Guo, W. Shen, Q. Xu, H. Liu, Y. Wang, B-doped carbon coating improves the electrochemical performance of electrode materials for Li-ion batteries, Adv. Funct. Mater. 24 (35) (2015) 5511–5521.
[43] J. Feng, Y. Wang, High-rate and ultralong cycle-life $LiFePO_4$ nanocrystals coated by boron-doped carbon as positive electrode for lithium-ion batteries, Appl. Surf. Sci. 390 (2016) 481–488.
[44] L. Wang, Y. Wang, M. Wu, Z. Wei, C. Cui, M. Mao, et al., Nitrogen, fluorine, and boron ternary doped carbon fibers as cathode electrocatalysts for zinc-air batteries, Small 14 (20) (2018) e1800737.
[45] J. Zhang, N. Nie, Y. Liu, J. Wang, F. Yu, J. Gu, et al., Boron and nitrogen codoped carbon layers of $LiFePO_4$ improve the high-rate electrochemical performance for lithium ion batteries, ACS Appl. Mater. Interfaces 7 (36) (2015) 20134–20143.
[46] L. Zhao, Y.S. Hu, H. Li, Z. Wang, L. Chen, Porous $Li_4Ti_5O_{12}$ coated with N-doped carbon from ionic liquids for Li-ion batteries, Adv. Mater. 23 (11) (2011) 1385–1388.
[47] X. Zhang, R.-S. Kühnel, H. Hu, D. Eder, A. Balducci, Going nano with protic ionic liquids—the synthesis of carbon coated $Li_3V_2(PO_4)_3$ nanoparticles encapsulated in a carbon matrix for high power lithium-ion batteries, Nano Energy 12 (2015) 207–214.
[48] C.J. Lv, X.C. Duan, J.W. Deng, T.H. Wang, $LiFePO_4$ mesocrystals coated with N-doped carbon from an ionic liquid for Li-ion batteries, CrystEngComm 19 (9) (2017) 1253–1257.
[49] Y. Meng, J. Xia, L. Wang, G. Wang, F. Zhu, Y. Zhang, A comparative study on $LiFePO_4$/C by in-situ coating with different carbon sources for high-performance lithium batteries, Electrochim. Acta 261 (2018) 96–103.
[50] J. Ni, Y. Zhao, J. Chen, L. Gao, L. Lu, Site-dependent electrochemical performance of Mg doped LiFePO4, Electrochem. Commun. 44 (2014) 4–7.
[51] F. Lu, Y. Zhou, J. Liu, Y. Pan, Enhancement of F-doping on the electrochemical behavior of carbon-coated $LiFePO_4$ nanoparticles prepared by hydrothermal route, Electrochim. Acta 56 (24) (2011) 8833–8838.
[52] E. Markevich, R. Sharabi, O. Haik, V. Borgel, G. Salitra, D. Aurbach, et al., Raman spectroscopy of carbon-coated $LiCoPO_4$ and $LiFePO_4$ olivines, J. Power Sources 196 (15) (2011) 6433–6439.
[53] J. Wu, G.K. Dathar, C. Sun, M.G. Theivanayagam, D. Applestone, A.G. Dylla, et al., In situ Raman spectroscopy of $LiFePO_4$: size and morphology dependence during charge and self-discharge, Nanotechnology 24 (42) (2013) 424009.
[54] R. Tian, H. Liu, Y. Jiang, J. Chen, X. Tan, G. Liu, et al., Drastically enhanced high-rate performance of carbon-coated $LiFePO_4$ nanorods using a green chemical vapor deposition (CVD) method for lithium ion battery: a selective carbon coating process, ACS Appl. Mater. Interfaces 7 (21) (2015) 11377–11386.
[55] C. Gao, J. Zhou, G. Liu, L. Wang, Lithium-ions diffusion kinetic in $LiFePO_4$/carbon nanoparticles synthesized by microwave plasma chemical vapor deposition for lithium-ion batteries, Appl. Surf. Sci. 433 (2018) 35–44.
[56] J. Aluha, S. Blais, N. Abatzoglou, Phase quantification of carbon support by X-ray photoelectron spectroscopy (XPS) in plasma-synthesized Fischer–Tropsch nanocatalysts, Catal. Lett. 148 (7) (2018) 2149–2161.
[57] Z. Wu, P. Li, Q. Qin, Z. Li, X. Liu, N-doped graphene combined with alloys (NiCo, CoFe) and their oxides as multifunctional electrocatalysts for oxygen and hydrogen electrode reactions, Carbon 139 (2018) 35–44.
[58] G. Ren, S. Li, Z.-X. Fan, J. Warzywoda, Z. Fan, Soybean-derived hierarchical porous carbon with large sulfur loading and sulfur content for high-performance lithium–sulfur batteries, J. Mater. Chem. A 4 (42) (2016) 16507–16515.
[59] T. Feng, W. Jiang, Z. Zong, M. Wu, Investigation of the electrochemical performance of polyvinylidene fluoride-derived $LiFePO_4$/C composite nanospheres, J. Mater. Sci. 53 (2) (2017) 1279–1285.
[60] G. Jo, S. Shanmugam, Single-step synthetic approach for boron-doped carbons as a non-precious catalyst for oxygen reduction in alkaline medium, Electrochem. Commun. 25 (2012) 101–104.
[61] Y. Zhao, L. Yang, S. Chen, X. Wang, Y. Ma, Q. Wu, et al., Can boron and nitrogen co-doping improve oxygen reduction reaction activity of carbon nanotubes? J. Am. Chem. Soc. 135 (4) (2013) 1201–1204.
[62] T. Kwon, H. Nishihara, H. Itoi, Q.H. Yang, T. Kyotani, Enhancement mechanism of electrochemical capacitance in nitrogen-/boron-doped carbons with uniform straight nanochannels, Langmuir 25 (19) (2009) 11961–11968.
[63] Y. Xu, K. Zhang, C. Brüsewitz, X. Wu, H.C. Hofsäss, Investigation of the effect of low energy ion beam irradiation on mono-layer graphene, AIP Adv. 3 (7) (2013) 072120.
[64] X. Liu, L. Dai, Carbon-based metal-free catalysts, Nat. Rev. Mater. 1 (11) (2016) 16064.
[65] G. Ren, S. Li, Z.-X. Fan, M.N.F. Hoque, Z. Fan, Ultrahigh-rate supercapacitors with large capacitance based on edge oriented graphene coated carbonized cellulous paper as flexible freestanding electrodes, J. Power Sources 325 (2016) 152–160.
[66] F. Cao, G.X. Pan, Y.J. Zhang, Construction of ultrathin N-doped carbon shell on $LiFePO_4$ spheres as enhanced cathode for lithium ion batteries, Mater. Res. Bull. 96 (2017) 325–329.
[67] S. Yoon, C. Liao, X.-G. Sun, C.A. Bridges, R.R. Unocic, J. Nanda, et al., Conductive surface modification of $LiFePO_4$ with nitrogen-doped carbon layers for lithium-ion batteries, J. Mater. Chem. 22 (11) (2012) 4611.
[68] H. An, Y. Li, Y. Gao, C. Cao, J. Han, Y. Feng, et al., Free-standing fluorine and nitrogen co-doped graphene paper as a high-performance electrode for flexible sodium-ion batteries, Carbon 116 (2017) 338–346.
[69] S.G. Peera, A.K. Sahu, A. Arunchander, S.D. Bhat, J. Karthikeyan, P. Murugan, Nitrogen and fluorine co-doped graphite nanofibers as high durable oxygen reduction catalyst in acidic media for polymer electrolyte fuel cells, Carbon 93 (2015) 130–142.
[70] M. Pan, X. Lin, Z. Zhou, Electrochemical performance of $LiFePO_4$/C doped with F synthesized by carbothermal reduction method using NH4F as dopant, J. Solid State Electrochem. 16 (4) (2011) 1615–1621.
[71] J. Li, L. Zhang, L.F. Zhang, W.W. Hao, H.B. Wang, Q.T. Qu, et al., In-situ growth of graphene decorations for high-performance $LiFePO_4$ cathode through solid-state reaction, J. Power Sources 249 (2014) 311–319.
[72] X. Xia, Y. Wang, D. Wang, Y. Zhang, Z. Fan, J. Tu, et al., Atomic-layer-deposited iron oxide on arrays of metal/carbon spheres and their application for electrocatalysis, Nano Energy 20 (2016) 244–253.
[73] X. Xia, Q. Xiong, Y. Zhang, J. Tu, C.F. Ng, H.J. Fan, Oxide nanostructures hyperbranched with thin and hollow metal shells for high-performance nanostructured battery electrodes, Small 10 (12) (2014) 2419–2428.